Characterization of the CO_2 microwave plasma based on the phenomenon of skin depth-limited contraction

A.J. Wolf,[†] T.W.H. Righart,[†] F.J.J. Peeters,[†] P.W.C. Groen,[†] M.C.M van de Sanden,[†,‡] and W.A. Bongers[*,†]

[†]*DIFFER - Dutch Institute for Fundamental Energy Research, De Zaale 20, 5612AJ Eindhoven, The Netherlands*

[‡]*Department of Applied Physics, Plasma Materials Processing group, Eindhoven University of Technology, P O Box 513, 5600 MB Eindhoven, The Netherlands*

E-mail: w.a.bongers@differ.nl

Abstract

The sub-atmospheric CO_2 microwave plasma is known to contract to a narrow filament with rising pressure as result of a mode transition. This changing state of contraction is investigated in relation to its dielectric properties, in order to directly relate the discharge parameters to the discharge radius. The electron density and gas temperature are measured, respectively, by 168 GHz microwave interferometry and Doppler broadening of the 777 nm oxygen emission lines. The plasma is operated in steady state with 1400 W at 2.45 GHz, between 100 mbar to 400 mbar. Electron density values in the central region range from 10^{18} to $10^{20}\,m^{-3}$ between the discharge modes, while the gas temperature increases from 3000 K to 6500 K, in good agreement with previously reported values. Based on the dielectric properties of the discharge in relation to the plasma radius, it is found that the discharge column constitutes a radius of a single skin depth. Implications of these insights on the conditions of previously reported CO_2 dissociation experiments are discussed.

Keywords: carbon dioxide, microwave plasma, contraction dynamics, skin-depth, electron density, microwave interferometry, gas conversion

1 Introduction

Plasma contraction, a phenomenon leading to filamentation or arcing, is widely observed in both DC and HF discharges in the moderate- to high pressure regime (10-1000 mbar). The contraction is related to the plasma parameters, such as power density, composition, temperature and electron density. A comprehensive contraction theory has been developed based on experimental work[1,2] and modeling.[3–6] The phenomenon of contraction in conditions of sub-atmospheric pressure is explained by an interplay between two essential mechanisms: a non-uniform heating mechanism, and enhanced dissociative recombination in the outer regions of the plasma.

The elevated temperatures inherently associated with the discharge contraction lead to an increase in the variety of species, particularly in molecular plasmas. This greatly complicates the charged particle kinetics of such systems. As a result, discharge contraction phenomena are well described by models in simple systems such as noble gases, while dedicated experimental and theoretical research is still required to understand the contraction dynamics in relation to the discharge properties for more complex molecular gases.[6] For discharges sustained in oscillating fields, it is proposed that the contracted plasma radius and the plasma parameters are directly related to the frequency-dependent skin-depth parameter.[1,7] While this notion of *skin depth-limited contraction* provides valuable insight into the plasma properties of such contracted plasma columns, conclusive experimental evidence has not yet been reported.

Contraction dynamics is a relevant topic for plasma-driven gas conversion applications such as CO_2 plasmolysis. In this context, the microwave discharge is iconic for its high plasma activation and is widely investigated for efficient large-scale plasma-chemical conversion.[8–15] High energy efficiencies of up to 80% have been reported by experimental investigation in a subsonic vortex-confined microwave reactor under proposed conditions of strong vibrational-translational (VT) nonequilibrium.[16–18] A comprehensive overview of these initial experiments and a theoretically grounded nonequilibrium interpretation is provided by Fridman[18] and Fridman and Kennedy[19]. The contraction dynamics of the CO_2 microwave plasma, which depends on the pressure, shows a strong correlation with optimized conditions for plasma activation of CO_2 in the pressure range of 100 mbar to 200 mbar. The influence of the contraction dynamics on the discharge parameters, however, remain ambiguous. The record efficiency values of 70% to 80%, obtained at a pressure of around 160 mbar, were reported to occur in conditions of strong radial contraction from a diffuse to a contracted discharge mode. Attempts to experimentally reproduce the energy efficiency achieved in the original experiments have so far been unsuccessful,[13–15] with reports generally showing thermal discharge conditions, characterized by high gas temperatures of over 3000 K and energy efficiencies below 50%. Interestingly, the optimal conditions in these experiments are also associated with a discharge transition.[13,14] Consequently, the maximum energy efficiencies for this collection of thermally interpreted conversion experiments were achieved at a similar pressure. This suggests that in both cases the contraction dynamics plays an important role in the dissociation.

In this paper, the contraction dynamics in a CO_2 microwave plasma is investigated, by relating the radius of the plasma to the dielectric properties of the plasma medium and the skin depth. The reactor configuration and plasma conditions in this work are chosen to

closely follow the operating conditions of Butylkin et al.[16] and related publications,[17,20] to facilitate a comparison with these results. The dimensions of the discharge modes of the plasma are established from its optical emission. The gas temperature and electron density are determined in the center of the plasma, through Doppler broadening measurements of the 777 nm O-line, and 168 GHz microwave interferometry, respectively. Apart from the electron density, the collision frequency of momentum transfer to neutral species ν_m also has a large influence on the dielectric properties of the plasma medium, and hence on the skin depth. Using the gas temperature, ν_m is calculated based on the anticipated composition in the discharge.

As we will show, the main result of this work is a direct experimental proof of the relation between the plasma radius and the skin depth: it is observed that the filament diameter of the microwave-sustained discharge is found to contract to a radius of approximately a single skin depth. Additionally, we assess the role of the vortex flow in the confinement of the plasma, since it has an important role in stabilizing the discharge in the center of the reactor tube. In light of these insights in the contraction dynamics, a critical discussion on the discharge parameters (i.e. gas temperature and electron density) in relation to the original high-efficiency results is provided, aiming to establish the extent of correspondence between discharge conditions.

2 Experimental set-up

A schematic of the plasma reactor is depicted in Fig. 1. The discharge is sustained with 2.45 GHz microwave field, which is applied with a shorted rectangular waveguide (WR-340). A quartz tube, transparent for microwaves, functions as the vacuum chamber. It intersects the center of the broad side of the waveguide, such that its axis is aligned with the field of the TE_{10} field mode. The discharge tube axis is positioned at a quarter guide wavelength from shorted end of the waveguide, so that the plasma coincides with a field maximum. A 3-stub tuner is used for impedance matching of the plasma to the source to minimize reflections back to the microwave source.

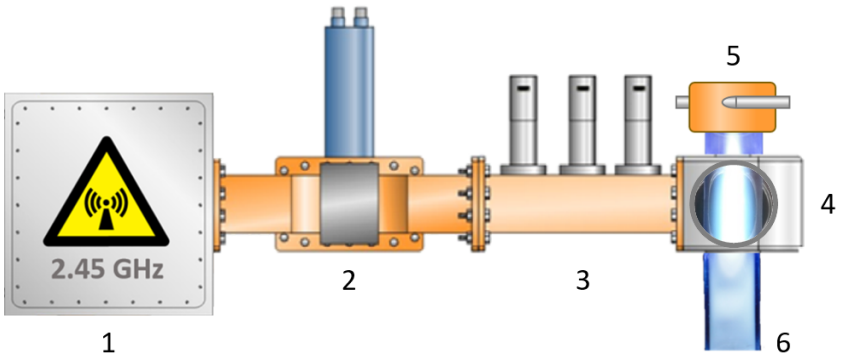

Figure 1: Illustration of the experimental setup, consisting of the microwave source (1), circulator (2), 3-stub impedance tuner (3) and the field applicator (4). The gas flow is tangentially injected (5) into the quartz reactor tube (6)

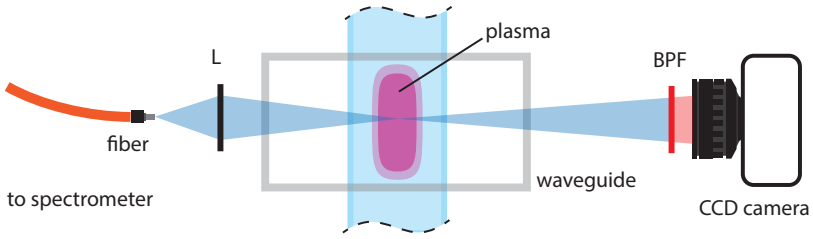

Figure 2: Illustration of the optical diagnostics setup (front-view). L: optical lens, BPF:band-pass filter.

A vortex flow is generated by tangentially injecting the gas in the injection plane (5) in Fig. 1. The vortex helps to stabilize the plasma in the center of the tube, which prevents damage to the quartz reactor wall. A detailed description of the experimental arrangement, and attained experimental results on the plasma-chemical conversion of CO_2, is provided by Bongers et al.[13].

The plasma width is defined as the full width at half maximum (FWHM) of the electron density profile. The radial electron density distribution in the plasma is derived from the intensity distribution of the 777 nm $O(3s^5S^0 \leftarrow 3p^5P)$ spectral line emission. A CCD camera is used to record the plasma emission, after isolating the spectral lines with a band-pass filter with a central wavelength around 780 nm, as illustrated in Fig. 2. The images and associated lateral emission intensity profiles of two typical plasma modes are shown in Fig. 3.

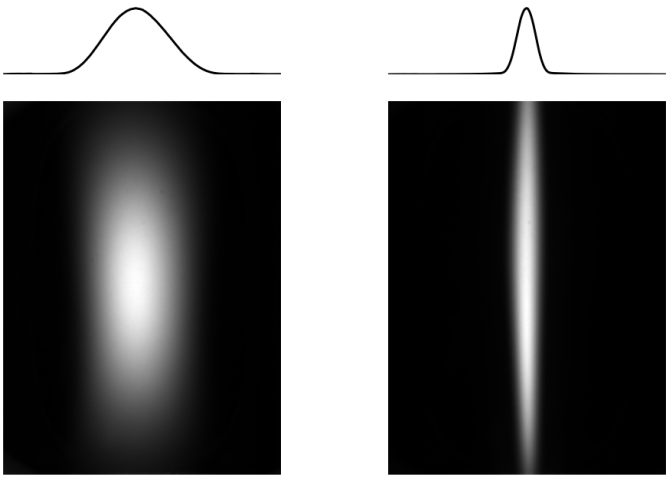

Figure 3: Recorded profiles of 777nm plasma emission for two distinct discharge modes: a diffuse mode at 100 mbar (left) and a contracted mode at 200 mbar (right). The intensity is normalized to maximize contrast.

The upper state of the 777 nm transition is mostly populated by electronic impact excitation, since the excitation energy of 10.74 eV far exceeds $k_B T_{\text{gas}}$. The emission intensity

scales with the population rate

$$I_{777} \propto n_e n_O k_{\text{ext}}(T_e) \propto n_e^s \tag{1}$$

with n_{O} the density of atomic oxygen, and $k_{\text{ext}}(T_e)$ the rate constant for electronic excitation (as motivated in App. A). The exponential scaling factor s has a value between 1 and 2, depending on the dominant production mechanism of atomic oxygen. In the extreme case that O formation is driven fully by neutral particle reactions, the rate depends on T_{gas} and the emission intensity scales with n_e ($s = 1$). On the other hand, when O formation follows from electron-impact reactions, such as electron impact dissociation, the emission intensity scales with n_e^2 ($s = 2$).

The relation between the plasma emission and electron density profile is illustrated in Fig. 4. The lateral plasma emission intensity profile is Gaussian. The characteristic width Λ_{777} is invariant under Abel transformation. Therefore, following Eq. (1) and assuming only slow radial variations in both T_{gas} and T_e with respect to the electron density, the radial n_e profile is expressed in terms of Λ_{777}:

$$n_e(r) = n_e(0) \exp\left(-\frac{1}{2}\frac{r^2}{(\sqrt{s}\Lambda_{777})^2}\right), \tag{2}$$

where $\Lambda_e = \sqrt{s}\Lambda_{777}$ is the characteristic width of the spatial density distribution. $n_e(0)$ is the peak value of the electron density, which will be determined later by microwave interferometry. Eq. 2 shows that the radial dimension of the plasma is identical or slightly larger than the spatial extent of the 777 nm intensity profile, depending on the exponential scaling parameter s. It is important to note that the n_e profile remains Gaussian under the influence the s, which is in agreement with numerical simulations other radially confined plasmas in (surface-wave sustained) microwave discharges.[4,21] According to our previous definition of the plasma width as the FWHM of the electron density profile, the discharge radius $r_{\text{pl}} = d_{\text{pl}}/2$ is expressed in terms of Λ_{777} as

$$r_{\text{pl}} := \Lambda_e\sqrt{2\ln 2} = \Lambda_{777}\sqrt{2s\ln 2} \qquad (1 \leq s \leq 2) \tag{3}$$

It will become apparent that this definition is convenient when relating the plasma dimensions to the skin-depth of the microwaves in the plasma.

The peak electron density on the discharge axis $n_e(0)$ is obtained from microwave interferometry using a quasi-optical free-space measurement approach similar to Bourreau et al.[22] at a fixed frequency of 168 GHz. The experimental configuration, which is based around a vector network analyzer (VNA), is illustrated in Fig. 5.

A custom millimeter-wave converter interfaces the VNA to the high frequency segment, by up- and down conversion of the signals by mixers and phase-locked local oscillators. A quasi-optical Gaussian beam path through the center of the discharge is realized by aligning two corrugated horn antennas with Teflon lenses on opposite sides of the reactor tube, perpendicular to the tube and plasma axis. Physical constraints imposed by the waveguide dimensions dictate a minimal distance between the horn antennas of 11 cm. The beam focus is positioned just before the plasma medium in a compromise between the size of the beam

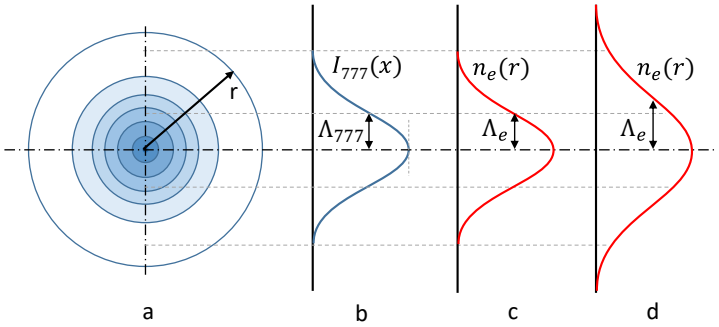

Figure 4: Illustration of a: the plasma emission profile cross section perpendicular to the plasma axis, b: the lateral projection of the 777 nm emission, c: the underlying n_e profile ($s = 1$) and d: the underlying n_e profile ($s = 2$).

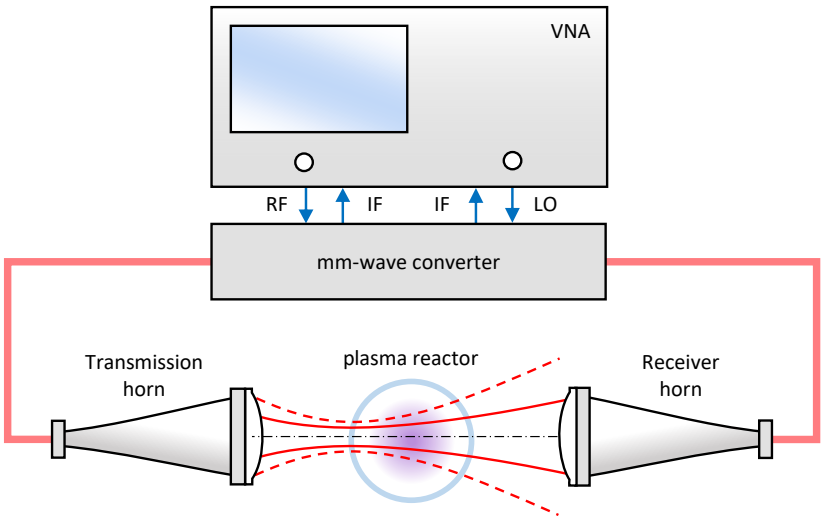

Figure 5: Illustration of the mm-wave measurement system, including the beam propagation path and alignment with respect to the plasma setup (viewed along the discharge axis).

waist and signal strength. A beam waist of 2 mm to 3 mm is realized, which is smaller or similar to the discharge diameter for the discharge conditions considered in this work. Therefore, a representative phase shift measurement is obtained, since most of the beam passes through the plasma.

The phase shifts $\Delta\phi$ induced by the plasma medium are determined by measuring the difference in phase between the "plasma-on" and "plasma-off" conditions in quick succession. Following this approach, the influence of the reactor tube and other surrounding features is accounted for, while also minimizing the effect of thermal drifts in the system associated with thermal expansion of the waveguides. We relate the phase shift to the dielectric properties of the plasma medium along the propagation path using the Lorentz conductivity model.[23] The complex refractive index of the plasma medium $\tilde{\mu}$ is described by the diagnostic angular frequency ω, the plasma frequency $\omega_\mathrm{p} = \sqrt{n_e e^2/\epsilon_0 m_e}$ in (rad s^{-1}) and the momentum transfer frequency ν_m (s^{-1}) between electrons and heavy species.

$$\tilde{\mu} = \mu + i\chi = \sqrt{1 - \frac{\omega_\mathrm{p}^2}{\omega(\omega - i\nu_\mathrm{m})}} \tag{4}$$

Here, μ and χ are the real and imaginary parts of $\tilde{\mu}$. In the near-field of the beam focus the plane wave approximation is used to describe the plasma medium as a slab with its spatially varying properties along the propagation path corresponding to the radial density profile of Eq. (2). In the high frequency limit ($\nu_c \ll \omega$), the refractive index is largely real and the dependence on collision frequency is negligible. The cumulative phase shift $\Delta\phi$ induced by the medium for a dielectric profile $\mu(x)$ is obtained by integration over the propagation path:[24]

$$\Delta\phi = \frac{c}{\omega}\int (1 - \mu(x))dx \tag{5}$$

The characteristic absorption length or skin depth, resulting in a $1/e$ attenuation of the field intensity, is determined by the from the complex part of the refractive index.

$$\delta = \frac{c}{\chi\omega} \tag{6}$$

For $\nu_\mathrm{m}/\omega \ll 1$ the medium acts as a low-loss dielectric medium with a skin depth $\delta = c/\omega_p$. In the collisional case, where ($\nu_\mathrm{m}/\omega > 1$), Eq. (6) takes the form of the well-known skin-effect in a conducting medium:[23]

$$\delta = \frac{c}{\omega_p}\sqrt{\frac{2\nu_\mathrm{m}}{\omega}} \approx \frac{c}{e}\sqrt{\frac{2m_e\epsilon_0}{\omega}\frac{\nu_\mathrm{m}}{n_e}} \tag{7}$$

The peak electron density along the propagation path $n_e(0)$ is determined for experimentally obtained values of $\Delta\phi$ and d_pl using Eq. (2) and (4) and solving Eq. (5).

As we will later show, the collisionless approach of Eq. (5) is justified since the momentum transfer frequency of the electrons in the center of the plasma is low in comparison to the diagnostic beam frequency. In this high frequency limit, *i.e.* ($\omega \gg \omega_\mathrm{p} \gg \nu_\mathrm{m}$), we expect a

low attenuation of the diagnostic beam and Eq. (5) can be written as an explicit function of the average electron density n_e integrated along the path of propagation:[23]

$$\Delta\phi = \int \frac{e^2}{2\omega_{\mathrm{d}} c m_e \epsilon_0} n_e(x) dx \tag{8}$$

Substitution of the experimentally obtained electron density profile function of Eq. (2) and rewriting for $n_e(0)$ gives

$$n_e(0) = \sqrt{\frac{2}{\pi}} \frac{\omega_{\mathrm{d}} c m_e \epsilon_0}{e^2} \frac{\Delta\phi}{\Lambda_e} \tag{9}$$

which provides a direct relation between phase shift and peak value of the electron density.

Using this approach, where the propagation is approximated by a plane wave through a plasma slab, reliable values of the electron density are obtained for our plasma conditions in the 50 mbar to 350 mbar pressure range. Below 50 mbar, the phase shift induced by the plasma is smaller than thermal fluctuations inherent to the detection method. In principle the upper measurement limit of the electron density is dictated by the cut-off at the critical electron density (which is $3.5 \times 10^{20}\,\mathrm{m}^{-3}$ at 168 GHz). We find however that upper measurement limit is rather limited by scattering effects, induced by the plasma column at resonant conditions of the wavelength in the plasma column $\lambda_d/\mu \approx d_{\mathrm{pl}}$, since the plane wave approximation breaks down under these circumstances. Further elaboration is provided in App. B.

The gas temperature is determined from the Doppler broadening of the 777 nm oxygen triplet emission lines, using a 3.3 pm resolution $f = 2.25$ m spectrometer in Littrow configuration. The collection optics have a focus of 0.9 mm and are aligned with the center of the discharge, as illustrated in Fig. 2. Since electronic excitation from the ground state is the dominant population mechanism for the upper state of this transition (see also App. A), the temperature of the excited state reflects that of the ground state species. The three spectral peaks are fitted with a Voigt profile. The gas temperature is determined from the Gaussian broadening component, after correcting for the instrument function. Other anticipated broadening effects such as Stark broadening and Van der Waals broadening are only minor, and since they lead to Lorentzian broadening components, do not affect the temperature value. The line-integrated measurements are most sensitive for the temperature in the center of the discharge since the emission intensity is highest in this region. Furthermore, flat temperature profiles are observed in lateral scans within the plasma region, which shows that the temperature is approximately constant over the discharge radius.

The ν_{m} value in the center of the discharge is calculated from the momentum transfer cross sections of the neutral species in the discharge. Since the degree of ionization n_e/n_0 generally does not exceed 10^{-4}, electron-ion contributions can be neglected. It remains important to consider the influence of composition and electron temperature since the variety of molecular excitation channels leads to momentum transfer cross sections that may vary greatly with both mean electron energy and composition.[25]

A general expression for collision frequency in multi-component mixtures, normalized to the neutral density, is obtained by summation over contributions from all major neutral

species in the discharge α.

$$\nu_{\mathrm{m}} \approx n_0 \sum_{\alpha} r^{(\alpha)} k_{e-\mathrm{n}}^{(\alpha)} \tag{10}$$

Here, $k_{e-\mathrm{n}}^{(\alpha)}$ are the rate constants for effective momentum transfer from electrons to heavy species, and $r^{(\alpha)}$ are the mole fractions of the neutral species α. The rate constants are calculated for each species as a function of electron temperature T_e by integrating the electron scattering cross-sections over an isotropic Maxwellian velocity distribution function of the electrons.[26]

$$k_{e-\mathrm{n}} = \int_0^{\infty} \frac{8\pi m_e E_e}{(2\pi m_e k_{\mathrm{B}} T_e)^{3/2}} \sigma(E_e) \exp\left(\frac{-E_e}{k_{\mathrm{B}} T_e}\right) dE_e \tag{11}$$

Here E_e is the center of mass energy of the electron. The recommended effective scattering cross-sections for momentum transfer are taken from the most recent version of the IST-database[27] (for CO_2, O_2 and O) and the Phelps Database (for CO). The assumption of a Maxwellian EEDF is justified, since deviations from the assumed Maxwellian EEDF have a minor influence on the ν_{m}. In contrast to processes with high threshold energy E_{th} such as electron impact ionization, which are driven by the tail of the EEDF when $E_{\mathrm{th}} \gg \langle E_e \rangle$, the process of momentum transfer of electrons to heavy particles is driven by the bulk of the EEDF. Therefore the value of ν_{m} is not sensitive to the shape (particularly the tail) of the EEDF.

An effective rate constant for momentum transfer in a gas mixture for low ionization degrees $\widetilde{k}_{e-\mathrm{n}}$ is defined,

$$\widetilde{k}_{e-\mathrm{n}} \approx \sum_{\alpha} r^{(\alpha)} k_{e-\mathrm{n}}^{(\alpha)}(T_e) \tag{12}$$

which accounts for the thermally induced composition shifts for a given pressure, temperature and electron temperature. Finally from Eq. (10) and (12) we obtain an expression of the collision frequency

$$\nu_{\mathrm{m}} \approx \widetilde{k}_{e-\mathrm{n}} \cdot n_0. \tag{13}$$

As will become apparent later, the T_{gas} is in the range of 3000 K to 6500 K in the considered pressure range. These high temperature values result in chemical reaction timescales similar to or shorter than the plasma residence time,[14,28] which can lead to a plasma composition that is determined by thermally driven neutral particle chemistry. Even so, plasma driven conversion processes such as electron impact dissociation, dissociative recombination, and dissociative attachment may also influence the chemical balance. These effects can only be quantified by elaborate modeling of the plasma kinetics and gas dynamics. Therefore we consider three plasma composition scenarios that represent the extreme cases:

1. The plasma consists of 100% CO_2, under the assumption that no conversion takes place
2. A mixture of CO and O in stoichiometric ratios, assuming full conversion to CO has occured in the plasma
3. The intermediate case where an chemical equilibrium composition has set in at temperature T_{gas} and plasma-assisted chemical conversion processes are neglected.

The mole fractions for the majority species under the chemical equilibrium conditions are obtained by minimizing the Gibbs free energy of the mixture at given pressure and temperature using the Cantera[29] single-phase equilibrium solver and the NASA Glenn thermochemistry dataset[30] for the majority species. The effective rate constant depends significantly on both T_{gas} and T_e. This is demonstrated by the calculations of $\widetilde{k}_{e-\mathrm{n}}$ in Fig. 6 for a fixed pressure of 100 mbar and several electron temperature values between 1 eV to 2 eV. The dependence of $\widetilde{k}_{e-\mathrm{n}}$ on the gas temperature demonstrates the effect of the thermodynamic equilibrium composition on the collisionality of the mixture.

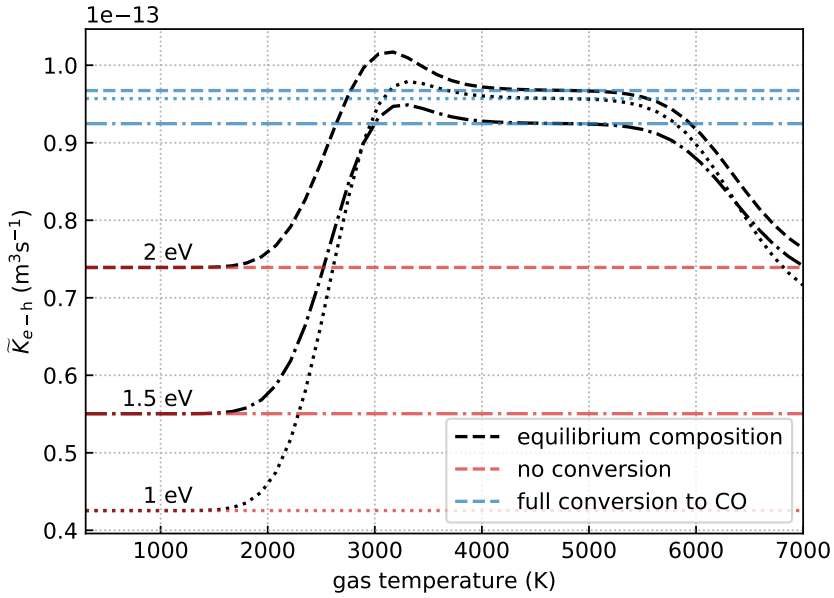

Figure 6: The effective rate constant for momentum transfer $\widetilde{k}_{e-\mathrm{n}}$ for different plasma compositions, calculated for the specified T_e values.

The calculations in Fig. 6 shows that $\widetilde{k}_{e-\mathrm{n}}$ does not depend strongly on either T_{gas} or T_e in mixtures with a high conversion to CO. In CO_2-rich mixtures on the other hand, $\widetilde{k}_{e-\mathrm{n}}$ is generally lower and more sensitive to T_e, since the effective momentum transfer cross section of CO is high in comparison to CO_2. For a wide range of plasma parameters, $T_{\mathrm{gas}} = 3000$ K to 6000 K and T_e values between $1 - 2$eV, the effective rate constant $\widetilde{k}_{e-\mathrm{n}} \approx 0.95 \times 10^{-13}$ m^{3}s^{-1} does not change significantly. This is convenient since in the present CO_2 plasmas, which are optimized for a high conversion to CO, the anticipated uncertainty range in the electron temperature does not have a large impact on ν_{m}.

3 Results

Fig. 7a shows the plasma radius r_{p}, and the corresponding core gas temperature T_{gas} in the pressure range of 50 mbar to 400 mbar. The input power and input flow rate were fixed at respectively 1400 W and 18 slm. We observe a significant reduction of the plasma radius, from approximately 7 mm to 2 mm, in the range of 100 mbar to 150 mbar, which

marks the characteristic discharge transition in CO_2 from the "diffuse" to the "contracted" conditions.[14,16,18,20] In the contracted regime, occurring above 150 mbar at higher pressure the discharge radius becomes constant for fixed power.

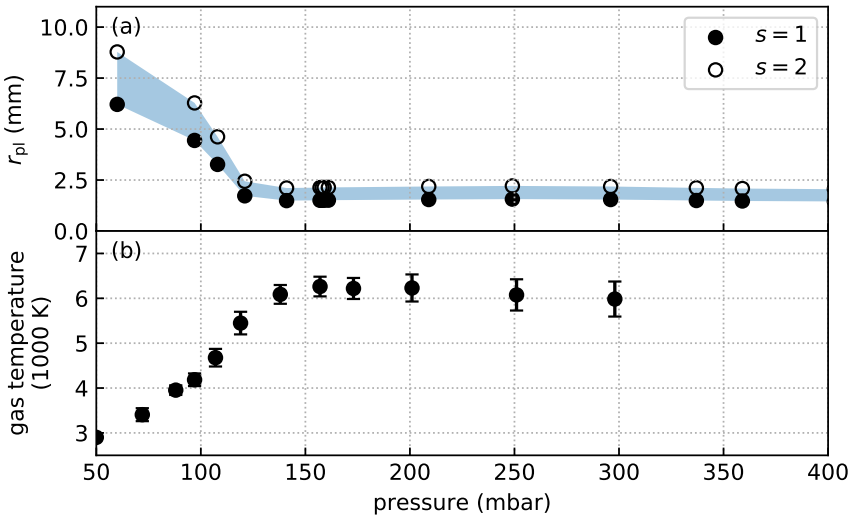

Figure 7: Experimental values of the discharge radius r_p and the gas temperature for 1400 W and 18 slm.

The core temperature shows a strong correlation with the plasma radius, which is expected based on the associated power density increase. The temperature measurements show a steep increase with pressure in the diffuse mode, from 3000 K to 4000 K, while in the contracted mode the temperature is only weakly related to the pressure with a range of 5500 K to 6500 K. The temperature values measured in this work agree well with previous values based on Rayleigh scattering[14] under similar discharge conditions.

The microwave interferometry measurements presented in Fig. 8 provide both the phase shift and attenuation data corresponding to the plasma conditions presented in Fig. 7. The collision frequency values are also provided, based on Eq. (12) and (13). This shows that $\nu_m/\omega_d \ll 1$ for the entire pressure range. Therefore, the plasma medium acts as a lossless dielectric medium with low attenuation. For higher pressures, however, we see an apparent deviation from this collisionless behavior as indicated by the non-zero attenuation. This effect can be attributed to a resonant, Mie-like scattering on the plasma column at pressures where the refractive index becomes sufficiently high. This scattering effect imposes an upper limit of approximately 350 mbar in the electron density analysis since the plane wave approximation used in the derivation of the electron density does not account for this effect. More details are provided in App. B.

The electron density obtained from Eq. (9) is plotted in Fig. 9 using the previous measurements of plasma radius and phase shift. The corresponding ionization degree is calculated with $n_0 = p/k_B T_{gas}$. We observe an electron density of $1 \times 10^{18}\,m^{-3}$ in the low pressure diffuse mode and $2 \times 10^{19}\,m^{-3}$ to $1 \times 10^{20}\,m^{-3}$ in the contracted mode. The change in the transition regime of 100 mbar to 125 mbar induces a shift in both electron density and ionization degree of more than an order of magnitude. In the contracted mode, we observe that the

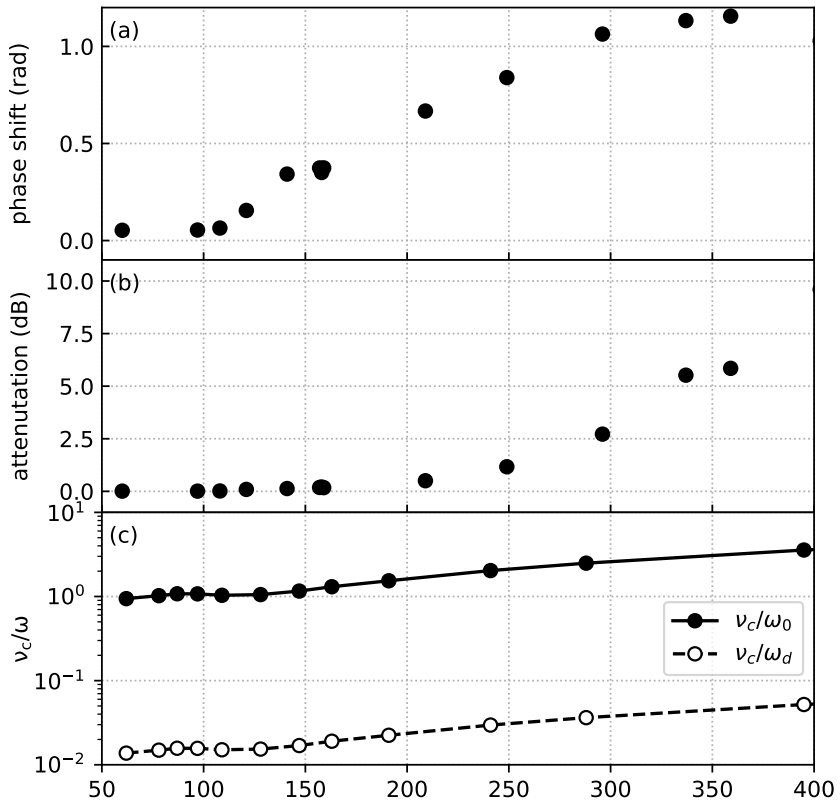

Figure 8: The wave propagation characteristics for the conditions of Fig. 7 in terms of phase shift (a) and attenuation (b). The collisionality of the discharge in relation with both the driving frequency ω_0 (2.45GHz) and the diagnostic frequency ω_d (168GHz) in the discharge core as function of pressure (c).

electron density scales linearly with pressure. Since the gas temperature only weakly changes with pressure in this regime, the ionization degree is found to remain constant with pressure for fixed power input. A comparison of the electron density values with measurements reported by Golubev and Tishchenko[20], which were obtained under comparable experimental conditions is included in Fig. 9(a). A good agreement is found, both in terms of absolute values and in terms of the pressure of transition. We note that relatively large errors towards $n_e = 10^{18}\,\mathrm{m}^{-3}$ are caused by a decline in signal to noise ratio of the phase shift measurement.

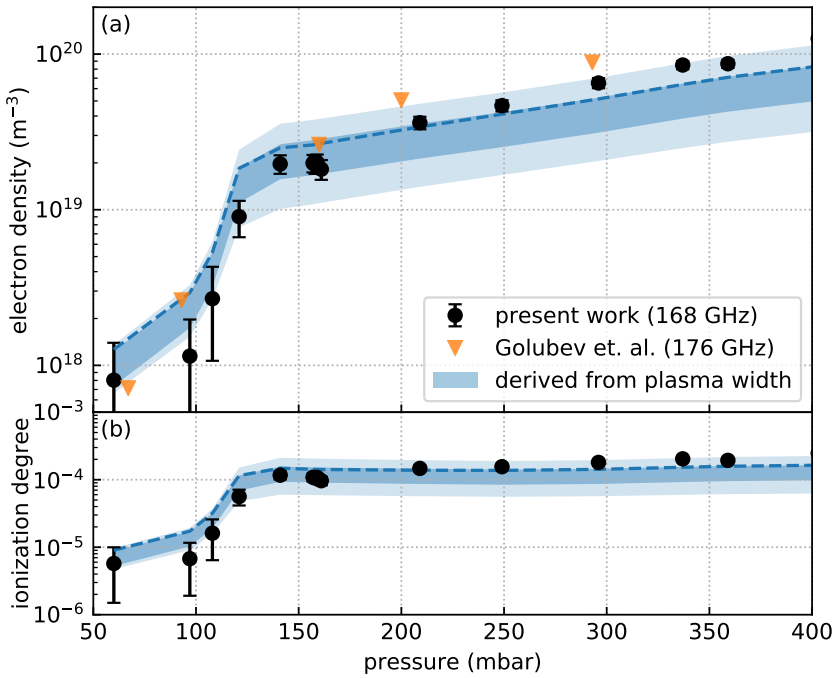

Figure 9: Experimental values of the electron density and associated ionization degree, based on the microwave interferometry and gas temperature measurements, and reference values obtained from Golubev and Tishchenko[20]. The blue markings indicate values derived from the skin-depth-limited contraction criterion ($s = 1$): assuming chemical equilibrium composition (dashed blue line), the range of no conversion to full conversion to CO (dark blue band), and its uncertainty band (light blue).

The effective skin-depth δ_{eff} in the core of the discharge corresponds well with the discharge radius. This is demonstrated by the normalized discharge radius parameter $r_{\mathrm{pl}}/\delta_{\mathrm{eff}}$, which is plotted in Fig. 10a as function of the electron density under the assumption of chemical equilibrium composition. The discharge radius is defined by Eq. (3) and δ_{eff} is calculated with Eq. (7). Since $r_{\mathrm{p}}/\delta_{\mathrm{eff}} \approx 1.0 \pm 0.3$ in the full electron density range, we postulate a condition of *skin-depth limited contraction*,

$$r_{\mathrm{pl}} := \delta_{\mathrm{eff}}. \tag{14}$$

which states that the plasma radius constitutes a single skin-depth. δ_{eff} can be described accurately by the collisional approximation of Eq. (7), since calculations in Fig. 8 show that

$\nu_c > \omega_0$ for both diffuse and contracted modes. Substitution of Eq. (7) and (13) into Eq. (14), and rewriting to the ionization degree gives

$$\frac{n_e}{n_0} \approx \frac{2 m_e \epsilon_0 c^2}{\omega_0 e^2} \frac{\widetilde{k}_{e-\mathrm{n}}}{r_{\mathrm{pl}}^2}, \tag{15}$$

which explicitly relates the ionization degree, electron density, discharge radius and gas temperature. The predictive power of the skin-depth-limited contraction criterion is demon-

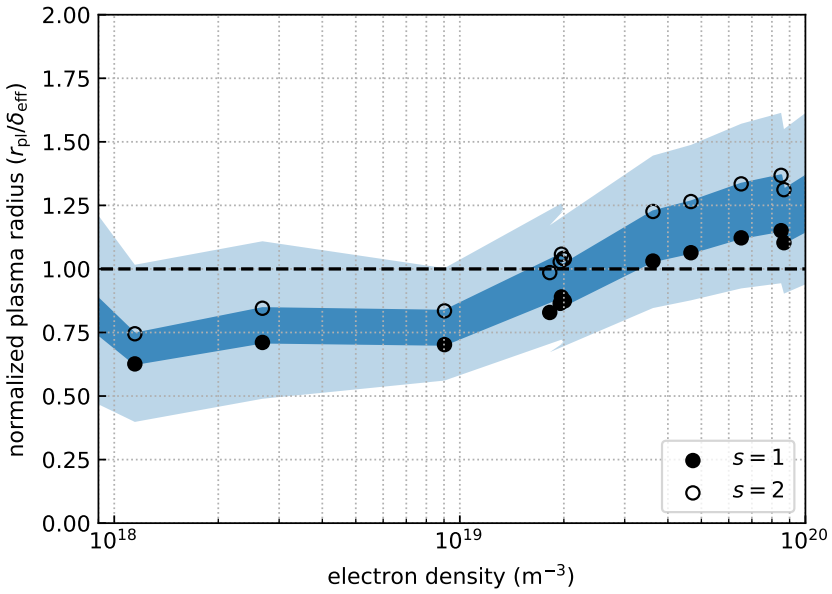

Figure 10: Ratio between the plasma radius r_{pl} and the effective skin-depth of the plasma δ_{eff}, as function of the measured peak electron density in the plasma core. Dark blue: value range resulting from exponential scaling factor s in the r_{pl} definition, and the associated uncertainty band (light blue).

strated by applying Eq. (15) to the values of Fig. 7, using $s = 1$. The results are plotted in Fig. 9 as blue lines for the previously described composition scenarios (i.e 100% CO_2, full conversion to CO and chemical equilibrium composition). In general, a good overlap is achieved for diffuse, contracted, and transition region, which shows that Eq. (15) captures the experimental values well. The experimental points fall roughly within the two extreme composition scenarios, for pure CO_2 (lower limit of the blue band) and full conversion to CO and O (upper limit). For pressures greater than 140 mbar, the values match under the assumption of a chemical equilibrium composition. At lower pressure, a high CO_2 concentration gives better agreement, which indicates that the conversion may be lower in this regime than predicted by the chemical equilibrium calculations. We note that a value of $s = 2$ may also alleviate the apparent discrepancy, since the measured n_e (Eq. 15) scales with $1/\sqrt{s}$, while the predicted value scales with $1/s$. As discussed previously, such deviations in composition and s value may occur as a result of plasma-enhanced reactivity (i.e. dissociative ionization, -attachment and -recombination). Gas-dynamic aspects such

as convective transfer may also result in deviations from chemical equilibrium composition. For instance, when $T_{\mathrm{gas}} < 3000\,\mathrm{K}$, the equilibration timescale of the heavy particle reactions become larger than the particle residence time,[14] which may lead to lower conversion and higher CO_2 concentrations in the plasma with respect to thermal chemical equilibrium. A more elaborate quantification of the composition in the plasma is out of the scope of this work but forms a topic of future research.

Rewriting Eq. (15) provides an expression of the discharge radius in terms of the ionization degree.

$$r_{\mathrm{pl}} \propto \sqrt{\frac{\widetilde{k}_{e-\mathrm{n}}}{\omega_0}\frac{n_0}{n_e}} \tag{16}$$

The calculations presented in Fig. 6 indicate that $\widetilde{k}_{e-\mathrm{n}}$ is approximately constant in the temperature range of 3000 K to 6000 K and electron temperatures ranging from 1 eV to 2 eV. In this case, the plasma radius is solely determined by the ionization degree and the driving frequency. This behavior is most evident in the contracted mode, where both the radius and ionization degree are constant and the temperature remains approximately constant with rising pressure. The constant ionization degree at constant input power can be explained based on the scenario of a recombination-controlled charged particle balance. In electropositive molecular discharges, at pressures where ambipolar diffusion can be neglected, ionization and dissociative recombination are balanced and the particle balance can be described by[19]

$$\frac{k_{\mathrm{iz}}(T_e)}{k_{\mathrm{dr}}(T_e)} = \frac{n_e}{n_0}. \tag{17}$$

Here k_{iz} and k_{dr} are the rate constants for direct impact ionization and dissociative recombination respectively. In this regime, the steady-state degree of ionization is uniquely determined by the electron temperature. Based on a presumed dominance of the CO molecule under chemical equilibrium conditions at 6000K, the observed ionization degree of $n_e/n_0 \approx 10^{-4}$ corresponds roughly to a constant electron temperature between 1.2 eV to 1.4 eV. The frequency dependence in Eq. (16) can be used to predict the implications of alternative driving frequencies on the plasma dimensions. A 915 MHz microwave in comparison to 2.45 GHz would entail a plasma radius that is a factor $\sqrt{2.45/0.915} = 1.6$ greater for otherwise identical temperature and ionization degree.

4 Discussion

To put the findings of this work in the context of current literature on contraction, we consider the influence of the plasma composition and the experimental configuration of the plasma source.

First, we assess the role of the gas-dynamic confinement, provided by the vortex flow, on the contraction behavior discussed above. The mechanisms of contraction relevant for molecular discharges in literature are mostly considered for wall-stabilized plasma columns. This stabilization mechanism relies on the radial heat transfer towards the wall via diffusion. The implications of gas-dynamic stabilization via convective heat transfer on the contraction

mechanism is not well established. The stabilizing effect of the vortex is often attributed to the transverse pressure gradient build-up induced by the centrifugal forces,[16,18] which would implicate a dependence of the plasma conditions on the specific flow dynamics of the present reactor configuration. It is reasoned that the resulting peak in E/n on axis determines the discharge burning region and governs its contraction. An opposing view is that the vortex only helps to stabilize the contracted plasma filament along the tube axis.[31] Our findings support this latter notion. Firstly the transverse pressure gradient is expected to be no more than 10%, as demonstrated by CFD modeling on a similar flow geometry.[32] The significant radial temperature buildup observed towards the discharge core[15] on the other hand suggests that the thermal-ionization contraction instability has a much greater influence on E/n via the inverse linear relationship between temperature and neutral density at isobaric conditions.

The role of vortex in the discharge contraction of the plasma is demonstrated with Helium. Reports on DC glow[6] and wall-stabilized microwave discharges[1] show that Helium exhibits little to no contraction in contrast to other noble gasses. This is attributed to a particularly weak contribution of molecular ion kinetics and associated recombination-driven contraction in Helium. The contraction behavior in the vortex-stabilized discharge is consistent with these literature reports, since we observe that even under conditions of intense vortex flow and high pressure the Helium discharge tends to remain in a diffuse state. Interestingly, the addition of trace amounts of water vapor leads to immediate contraction, which provides strong evidence that the crucial role of molecular ions in the contraction process for wall-stabilized discharges also applies in vortex stabilized discharges.

Based on this qualitative agreement, the contraction phenomena observed in vortex-confined discharges and wall-stabilized discharges likely share the same underlying contraction mechanisms. Kabouzi et al.[1] proposes axisymmetric heat transfer as a prerequisite for stabilization of discharge filaments that are subject to thermal heating instability. The stabilizing and confining effect of the vortex flow, therefore, appears to be a result of the enhanced symmetric radial heat transfer it imposes rather than radial pressure gradients induced by the centrifugal forces.

Since the universal nature of the skin depth as an absorption length-scale for oscillating fields in dielectric media, we can speculate whether the *skin depth-limited contraction* in CO_2 can be extended to other gases subject to contraction (*i.e.* in most molecular and electronegative gases and most noble gases[7]). Following the discussion above, the contraction mechanisms in vortex-stabilized CO_2 plasma are arguably governed by the same contraction mechanisms as other discharges reported in literature. Furthermore, results in this paper show that the *skin depth-limited contraction* applies for both discharge modes of the CO_2 microwave plasma. The distinct temperatures associated with these discharge modes essentially result in different gas mixtures since the composition changes associated with thermal decomposition are known to lead to significant changes in charged particle kinetics.[33] The fact that CO_2 shows a uniform behavior across the discharge modes emphasizes that skin depth-limited contraction is a general phenomenon for contracted discharges, basically independent of gas species and charged particle kinetics.

Table 1 provides a summary of experimentally obtained temperature measurements and overall energy efficiency η reported for various CO_2 microwave discharges. The gas temperature measurements reported in this work are consistent with many reports in a broad

Table 1: Summary of reported temperature measurements for several steady state CO_2 microwave plasmas in various configurations, over a wide range of plasma conditions. The driving frequency is 2.45 GHz unless otherwise indicated.

power (W)	pressure (mbar)	T_{gas} (K)	T_{vib} (K)	SEI (eV/mol)	η %	specification	measurement method	reference
1400	80	4000		1	(<40)	vortex	Doppler	this work
1400	150	6200		1	(<40)	vortex	Doppler	this work
800	127	4000		1	48	vortex	Rayleigh	[14]
554	212	5000		0.6	40	vortex	Rayleigh	[14]
830	53	2780		0.9	27	vortex	Rayleigh	[14]
5000	200	5700	9000 (1)	0.9	48	vortex (2)	C_2-Swan	[13]
1000	200	4000	9000 (1)	0.9	40	vortex	C_2-Swan	[13]
80	160	3000		0.6	10	vortex	Raman	[37]
2000	1000	6710		2.8		torch	OH emission	[34]
3000	1000	5000-6760		2.8		torch	C_2-swan	[36]
2000	1000	6200	6200	1.4-5.5		torch	C_2-swan	[35]
1750 (3)	160	300-1500	4000	0.9	80	vortex	several	[16]

(1) vibrational temperature based on C_2-swan emission fits is likely over-estimated
(2) a deviating frequency of 915 MHz was used
(3) discharge power likely over-estimated due to impedance mismatch

range of experimental conditions. Gas temperature values of 3000 K to 6000 K are typically observed in the moderate pressure regime, based on measurements of C_2 Swan-band emission,[13] Rayleigh scattering[14] and Raman spectroscopy.[15] Extended to the conditions of higher pressure, the temperatures values correspond well to the temperature values of 5000 K to 7000 K reported for CO_2 plasma torch flames at atmospheric pressure.[34–36] The efficiency values are consistent with heavy particle kinetics calculations provided by den Harder et al.[14], which show that an efficiency of up to approximately 50% can be achieved only for gas temperatures above 3000K.

The reports of Butylkin et al.[16] and related works[20,38,39] stand out with respect to the other temperature values in Table 1. A record energy efficiency value of 80% was found at a relatively low gas temperature of <1500 K. In the core of the discharge, Butylkin et al.[16] reports a state of high VT-nonequilibrium, marked by a vibrational temperature of 4000 K and a rotational temperature of 300 K to 1000 K. Both these values were obtained by spectral fitting of the ro-vibrational CO_2 peaks at 2.5 µm to 3.1 µm. In addition, the rotational temperature of 1500 K was determined based on the emission spectra for the ro-vibrational bands of the C_2-swan bands. It is notable that also a CN-swan system emission profile was obtained that indicated a gas temperature of 4000 K, much closer to the thermal conditions observed in our experiments. This value was however disqualified by the authors of this paper based on a presumed lack of equilibration between the rotational and translational temperature. In the following discussion, the insights obtained in this work regarding the electron density, gas temperature and contraction behavior obtained are used to reevaluate the reported plasma conditions of CO_2 conversion in relation to high efficiency conversion.

The electron densities reported by Golubev and Tishchenko[20], which are closely related

to the high-efficiency experiments reported by Butylkin et al.[16] show good agreement with our results in Fig. 9. The electron density is found to agree in both the low pressure and high pressure conditions. Also, the transition dynamics between the discharge modes coincides, marked by the strong increase of electron density with pressure around the transition pressure of 100 mbar to 150 mbar. Only minimal information has been reported on the plasma dimensions in the original set of experiments: plasma diameters of 20 mm and 6 mm are reported, respectively, for the diffuse and contacted mode.[18] A direct quantitative comparison between these values and our results is not possible since the exact experimental conditions used to obtain these values are unknown. It does show, however, that the plasmas were in varying states of contraction for rising pressure, similar to our observations. The agreement of the electron density, the coincidence of discharge modes with pressure and the similarities in the contracted size demonstrates that the contraction dynamics encountered in both experiments are very similar.

In light of the underlying mechanisms of contraction, which were discussed previously (governed by a thermal-ionization instability), it is unclear if the observed contraction behavior can be accounted for without significant heating of the discharge core. Furthermore, the optical emission features originating from C_2 recorded in the high-efficiency discharges may indicate conditions of high temperature in the discharge core. The presence of C_2 emission is known to be linked to the thermodynamic equilibrium composition:[40] the temperature range of C_2-swan emission measurements in plasma mixtures of $CH_4/CO_2/Ar$ was limited to the region of highest thermodynamic equilibrium concentration of C_2. In CO_2 the C_2 concentrations reaches highest concentrations at 5000 K to 7000 K and drop off rapidly for lower temperatures. Therefore, the presence of C_2 emission in the CO_2 spectrum is expected under chemical equilibrium conditions at gas temperature values of at least 5000 K. This appears to agree with the fact that we observe C_2 emission only in the contracted mode where the gas temperatures exceed this threshold value. It is therefore plausible that the presence of C_2-Swan emission in itself indicates conditions of high temperature in the discharge. Further investigation on the relation between C_2-Swan emission intensity and gas temperature and thermodynamic equilibrium composition is required to further assert this notion.

Based on the similarities identified in the contraction behavior, combined with the reported presence of C_2 features in the emission spectrum, it is plausible that the core (translational) temperature of the plasma core reported by Butylkin et al.[16] was significantly underestimated for the 80% efficiency results. This would entail a more dominant contribution of thermal conversion also in these high-efficiency CO_2 conversion results than has been previously recognized. High efficiency values may be explained also by a dominant contribution of thermal dissociation in combined with an optimized cooling product quenching trajectory.[15] Super-ideal quenching (where reactive oxygen formed in the core reacts with vibrationally excited CO_2 to form CO) and nonequilibrium contributions that may arise at the interface of the hot plasma region and the cold surroundings may contribute to an overall efficiency of up to 80%.[15] This notion not only provides a more consistent picture in relation to the plasma core parameters reported recently but also highlights the potential gains that can be made by optimizing the quenching trajectory of the products around the plasma. The effect of flow dynamics on particularly the quenching trajectory however currently remains a largely unexplored topic of research. In this regard, future studies on optimization of the reactor conditions for efficient CO_2 conversion should focus on understanding the role of gas

dynamics and product quenching rather than the plasma core parameters.

5 Conclusions

In this work, we studied the radial contraction of the sub-atmospheric pressure CO_2 microwave discharge and its effect on the discharge parameters. The objective was to establish a direct relationship between the discharge radius and the skin depth of wave absorption, by means of the dielectric parameters of the plasma medium.

We find that the CO_2 microwave plasma filaments in the radially contracted states have a radius that constitutes approximately one skin depth. The radius of the discharge is governed by the ionization degree and collision frequency in the plasma medium. Based on this insight we demonstrate that the ionization degree can be successfully derived from the radius of the discharge when the gas temperature and the composition are known. The results apply both to the diffuse and contracted discharge modes of the CO_2 microwave plasma and can be generalized to collisional discharges sustained in high frequency fields and subjected to radial contraction or filamentation.

The discharge contraction is explained by the thermal-ionization instability, which suggests that non-homogeneous gas heating is essential to explain the occurrence of the discharge modes. Obtained insights in the plasma parameters and the observed contraction dynamics are consistent with several key reports on the conversion of CO_2 in microwave plasmas. This underlines the similarities between these discharges and also the importance of thermally driven dissociation to explain the high energy efficiency. The occurrence of the discharge modes can not be fully explained since the complex interplay between the charged particle kinetics, heating and reactivity are currently not well understood. The importance of controlling the discharge modes in optimizing the plasma processing conditions motivates further investigation on the contraction dynamics.

Acknowledgement

This research has been carried out as part of the Plasma Power to Gas research program with reference 13581, which is co-financed by the Netherlands Organization for Scientific Research (NWO) and Alliander N.V. In addition, this work has received funding from the European Union's Horizon 2020 Research and Innovation Programme under GA-Nr 763909. The authors would like to acknowledge Jelke Toonen for his valuable contribution in assembling and commissioning the microwave interferometry setup.

References

(1) Kabouzi, Y.; Calzada, M. D.; Moisan, M.; Tran, K. C.; Trassy, C. Radial contraction of microwave-sustained plasma columns at atmospheric pressure. *Journal of Applied Physics* **2002**, *91*, 1008–1019.

(2) Dyatko, N. A.; Ionikh, Y. Z.; Kochetov, I. V.; Marinov, D. L.; Meshchanov, A. V.; Napartovich, A. P.; Petrov, F. B.; Starostin, S. A. Experimental and theoretical study

of the transition between diffuse and contracted forms of the glow discharge in argon. *Journal of Physics D: Applied Physics* **2008**, *41*, 055204.
(3) Raizer, Y. P. *Gas discharge physics*; Springer-Verlag: Berlin, 1991.
(4) Martinez, E. C.; Kabouzi, Y.; Makasheva, K.; Moisan, M. Modeling of microwave-sustained plasmas at atmospheric pressure with application to discharge contraction. *Physical Review E - Statistical, Nonlinear, and Soft Matter Physics* **2004**, *70*, 1–12.
(5) Ridenti, M. A.; De Amorim, J.; Dal Pino, A.; Guerra, V.; Petrov, G. Causes of plasma column contraction in surface-wave-driven discharges in argon at atmospheric pressure. *Physical Review E* **2018**, *97*, 1–14.
(6) Golubovskii, Y. B.; Nekuchaev, V.; Gorchakov, S.; Uhrlandt, D. Contraction of the positive column of discharges in noble gases. *Plasma Sources Science and Technology* **2011**, *20*, 053002.
(7) Moisan, M.; Pelletier, J. *Journal of Chemical Information and Modeling*; 2012.
(8) Spencer, L. F.; Gallimore, A. D. Efficiency of CO2 dissociation in a radio-frequency discharge. *Plasma Chemistry and Plasma Processing* **2011**, *31*, 79–89.
(9) Spencer, L. F.; Gallimore, A. D. CO2 dissociation in an atmospheric pressure plasma/catalyst system: a study of efficiency. *Plasma Sources Science and Technology* **2013**, *22*, 015019.
(10) Goede, A.; Bongers, W.; Graswinckel, M.; van de Sanden, M.; Leins, M.; Kopecki, J.; Schulz, A.; Walker, M. Production of solar fuels by CO2 plasmolysis. *EPJ Web of Conferences* **2014**, *79*, 1005.
(11) Silva, T.; Britun, N.; Godfroid, T.; Snyders, R. Optical characterization of a microwave pulsed discharge used for dissociation of CO 2. *Plasma Sources Science and Technology* **2014**, *23*, 025009.
(12) Kozák, T.; Bogaerts, A. Evaluation of the energy efficiency of CO2 conversion in microwave discharges using a reaction kinetics model. *Plasma Sources Science and Technology* **2014**, *24*, 015024.
(13) Bongers, W. A. et al. Plasma-driven dissociation of CO 2 for fuel synthesis. *Plasma Processes and Polymers* **2017**, *14*, 1600126.
(14) den Harder, N.; van den Bekerom, D. C. M.; Al, R. S.; Graswinckel, M. F.; Palomares, J. M.; Peeters, F. J. J.; Ponduri, S.; Minea, T.; Bongers, W. A.; van de Sanden, M. C. M.; van Rooij, G. J. Homogeneous CO 2 conversion by microwave plasma: Wave propagation and diagnostics. *Plasma Processes and Polymers* **2017**, *14*, 1600120.
(15) van den Bekerom, D. C. M.; Linares, J. M. P.; Verreycken, T.; van Veldhuizen, E. M.; Nijdam, S.; Berden, G.; Bongers, W. A.; van de Sanden, M. C. M.; van Rooij, G. J. The importance of thermal dissociation in CO 2 microwave discharges investigated by power pulsing and rotational Raman scattering. *Plasma Sources Science and Technology* **2019**, *28*, 055015.
(16) Butylkin, Y.; Zhivotov, V.; Krasheninnikov, E.; Krotov, M.; Rusanov, V.; Tarasov, Y.; Fridman, A. Dissociation of CO2 by a plasma-chemical process in a nonequilibrium microwave discharge. *Sov. Phys. Tech. Phys.* **1981**, *26*, 555.
(17) Asisov, R.; Givotov, V.; Krasheninnikov, E.; Potapkin, B.; Rusanov, V.; Fridman, A. Carbon dioxide dissociation in non-equilibrim plasma. 1983.
(18) Fridman, A. *Plasmas Chemistry*; Cambridge University Press, 2008.

(19) Fridman, A.; Kennedy, L. A. *Plasma Physics and Engineering*; 2004; pp 3–231.
(20) Golubev, A.; Tishchenko, E. Electron density and effective collision frequency measurements in CO2 UHF-discharge by microwave diagnostic techniques. 1981.
(21) Ikegami, H. Scattering of Microwaves from a Plasma Column in Rectangular Waveguide. *Japanese Journal of Applied Physics* **1968**, *7*, 634–655.
(22) Bourreau, D.; Péden, A.; Le Maguer, S. A quasi-optical free-space measurement setup without time-domain gating for material characterization in the W-band. *IEEE Transactions on Instrumentation and Measurement* **2006**, *55*, 2022–2028.
(23) Heald, M.; Wharton, C. B. *Plasma Diatnostics with Microwaves*; Wiley, 1965.
(24) Akhtar, K.; Scharer, J. E.; Tysk, S. M.; Kho, E. Plasma interferometry at high pressures. *Review of Scientific Instruments* **2003**, *74*, 996–1001.
(25) Schulz, G. J. *Resonances in Electron Impact on Diatomic Molecules" I. Introduction A. Classification of Compound States*; 1973; Vol. 45; pp 423–486.
(26) Mitchell, J. B. A.; Hus, H. The dissociative recombination and excitation of CO+. *Journal of Physics B: Atomic and Molecular Physics* **1985**, *18*, 547–555.
(27) Alves, L. L. The IST-LISBON database on LXCat. *Journal of Physics: Conference Series* **2014**, *565*, 012007.
(28) Gutsol, A.; Rabinovich, A.; Fridman, A. Combustion-assisted plasma in fuel conversion. *Journal of Physics D: Applied Physics* **2011**, *44*, 274001.
(29) Goodwin, D. G.; Moffat, H. K.; Speth, R. L. Cantera: An Object-oriented Software Toolkit for CHemical Kinetics, Thermodynamics adn Transport Processes. 2017; `http://www.cantera.org`.
(30) McBride, B.; Zehe, M.; Gordon, S. NASA Glenn coeefficients for calculating thermodynamic properties of individual species. *NASA* **2002**, 287.
(31) Fleisch, T.; Kabouzi, Y.; Moisan, M.; Pollak, J.; Castãos-Martínez, E.; Nowakowska, H.; Zakrzewski, Z. Designing an efficient microwave-plasma source, independent of operating conditions, at atmospheric pressure. *Plasma Sources Science and Technology* **2007**, *16*, 173–182.
(32) Trenchev, G.; Kolev, S.; Bogaerts, A. A 3D model of a reverse vortex flow gliding arc reactor. *Plasma Sources Science and Technology* **2016**, *25*, 035014.
(33) Wang, W.; Bogaerts, A. Effective ionisation coefficients and critical breakdown electric field of CO2 at elevated temperature: Effect of excited states and ion kinetics. *Plasma Sources Science and Technology* **2016**, *25*, 055025.
(34) Kwak, H. S.; Uhm, H. S.; Hong, Y. C.; Choi, E. H. Disintegration of Carbon Dioxide Molecules in a Microwave Plasma Torch. *Scientific reports* **2015**, *5*, 18436.
(35) Sun, H.; Lee, J.; Do, H.; Im, S. K.; Soo Bak, M. Experimental and numerical studies on carbon dioxide decomposition in atmospheric electrodeless microwave plasmas. *Journal of Applied Physics* **2017**, *122*.
(36) Chun, S.; Shin, D.; Ma, S.; Yang, G.; Hong, Y. CO2 Microwave Plasma—Catalytic Reactor for Efficient Reforming of Methane to Syngas. *Catalysts* **2019**, *9*, 292.
(37) van den Bekerom, D. C. M. Vibrational excitation for efficient chemistry in CO2 microwave plasmas. Dissertation, University of Technology, Eindhoven, 2018.
(38) Legasov, V. A.; Zhivotov, V. K.; Krasheninnikov, E. G.; Krotov, M. F.; Patrushev, L.; Rusanov, V. D.; Rykunov, G. V.; Spektor, A. M.; Fridman, A. A.; Sholin, G. V. A nonequilibrium plasma-chemical process of CO2 dissociation in high-frequency and

ultra-high-frequency discharges. *Soviet Physics Doklady* **1978**, *23*, 44–46.
(39) Rusanov, V.; Fridman, A.; Sholin, G. The physics of a chemically active plasma with nonequilibrium vibrational excitation of molecules. 1981.
(40) Nassar, H. C2 Swan spectrum used as a molecular pyrometer in transferred arc and the influence noise to signal ratio on the temperature values. *Journal of Physics: Conference Series* **2014**, *511*.
(41) Dagdigian, P. J.; Forch, B. E.; Miziolek, A. W. Collisional transfer between and quenching of the 3p 3P and 5P states of the oxygen atom. *Chemical Physics Letters* **1988**, *148*, 299–308.
(42) Groen, P. W. C.; Wolf, A. J.; Righart, T. W. H.; van de Sanden, M. C. M.; Peeters, F. J. J.; Bongers, W. A. Numerical model for the determination of the reduced electric field in a CO 2 microwave plasma derived by the principle of impedance matching. *Plasma Sources Science and Technology* **2019**, *28*, 075016.
(43) Balanis, C. *Advanced Engineering Electromagnetics*, 2nd ed.; Wiley, 2012.

A Derivation of the electron density shape

The 777 nm lines are excited mostly via direct electron impact excitation from the ground state. The excitation energy of $10.74\,\mathrm{eV} > T_e > T_{\mathrm{gas}}$ and the effective collisional quenching of excited states in the moderate pressure regime of this work make excitation via stepwise- or heavy-particle induced processes less likely. In this case the radiation balance can in this can be expressed as:

$$\mathcal{I}_{777nm} \propto n_{\mathrm{O}}^{*} k_{\mathrm{rad}} \approx k_{\mathrm{rad}} \frac{k_{\mathrm{ext}}(T_e) \cdot n_O n_e}{k_{\mathrm{rad}} + n_0 k_{Q,M}} \tag{A1}$$

Here, $k_{\mathrm{ext}}(T_e)$ is the rate constant of electronic excitation, n_O is the atomic oxygen ground state density. The proportionality of n_e with $\mathcal{I}_{777}$ is evaluated by assessing the timescales involved in the process. The radiative lifetime $\tau_{rad} = 1/k_{\mathrm{rad}}$ of the upper state is approximately 50 ns.[41] The rate constant of collisional quenching of the upper state by heavy particle interactions $k_{\mathrm{Q}} \approx 10.8 \cdot 10^{-16} \mathrm{m^3 s^{-1}}$ [41] and electron-induced quenching can be neglected at low ionization degree. Since k_{Q} and k_{rad} are constants and $k_{\mathrm{Q}} n_0 > k_{\mathrm{rad}}$ using typical plasma conditions, the radial emission intensity profile becomes a function of electron temperature, mole fraction of ground state oxygen and the electron density.

$$\mathcal{I}_{777\mathrm{nm}} \propto k_{\mathrm{ext}}(T_e) \cdot x_O \cdot n_e \tag{A2}$$

While the electrons are bounded by as a result of the contraction dynamics, the spatial distributions of temperature and species concentrations are expected to be more expanded. Therefore, if heavy particle conversion dominates in the plasma it is reasonable to assume that the mole fraction of oxygen x_O is independent of n_e and varies slowly with respect to the electron density. In the scenario where atomic oxygen is driven by electron-impact reactions, the oxygen density is directly proportional to the electron density, which would entail an n_e^2 dependence in Eq. (A1). The radial dependence of E/n_0 is expected change slowly with electron density within the plasma medium, since the influence of temperature rise and attenuation of the field towards the center of the filament have counteracting effect on E/n.[18] This is supported by simulations of wave absorption in the plasma medium.[42]

Significant influence of the rate constant $k_{\mathrm{ext}}(T_e)$ can be expected due to its exponential dependence on E/n. Since proper accounting for this effect would involve extensive self-consistent modeling of the discharge contraction kinetics, we assume the E/n_0 is constant over the entire discharge radius. The implication of this assumption is that the electron density is may be somewhat over- or underestimated as a result of the possible radial dependence of E/n_0. It is important to note that the definition of the discharge radius, arbitrary in nature, may have a more significant impact.

Therefore, it is reasonable to adopt the approximation

$$\mathcal{I}_{777} \propto n_e^{\mathrm{s}} \quad (1 \leq s \leq 2), \tag{A3}$$

which assumes constant T_{gas} and T_e along the discharge radius, and accounts for the anticipated effect of shifting dominant oxygen production mechanisms with the exponential scaling parameter s. The radial emission intensity has a Gaussian profile which is described

by

$$\mathcal{I}_{777}(r) = \mathcal{I}_{777}(0) \exp\left(-\frac{1}{2}\frac{r}{\Lambda_{777}}\right), \tag{A4}$$

where $\mathcal{I}_{777}(0)$ is the emission intensity on the discharge axis and Λ_{777} is the standard deviation. The Gaussian radial electron density profile of Eq. (2) is obtained from Eq. (A3) and (A4), which agrees well with Gaussian profiles obtained via numerical simulations of the electron density profile in similar discharges.[4,21]

B Limitation on the derivation of the electron density

The electron density calculations using Eq. (9) are based on the plane wave propagation through a dielectric medium using the Lorentz conductivity model. This expression is derived based on the homogeneous slab approximation and the adiabatic approximation.

- In the homogeneous slab approximation the problem is simplified to a plane wave propagation calculation through an infinite plasma slab geometry. In our case, the electron density variation along the propagation axis corresponds with the radial density profile. For large homogeneous plasma conditions where the plasma size is much larger than the diagnostic wavelength, the homogeneous approximation is valid. Significant deviations from ideal behavior are expected at high ionization degrees due to scattering effects when the diagnostic wavelength approaches the plasma diameter.

- The collisionless approximation, it is assumed that no absorption in the plasma medium occurs. This approximation is valid when when $\nu_\mathrm{m}/\omega_\mathrm{d} \ll 1$ and the plasma frequency is lower than the diagnostic frequency.[23]

Since the plasma has a cylindrical geometry rather than a slab, and the radius of the discharge approaches the wavelength of the diagnostic beam (1.8 mm), it is important to establish the boundaries at which the assumptions break down. We therefore assess in this section the applicability of Eq. (9) for the plasma conditions presented in this work.

The ideal collisionless behavior is demonstrated by assessing the ratio of phase shifts from the dual frequency phase shift ratio analysis. According to the ideal behavior in Eq. (9) the ratio between the acquired phase shifts for the distinct frequencies should equal collisionless ratio of the diagnostic frequencies. A deviation from this ideal behavior can indicate, for instance, unaccounted collisional effects. Fig. 11 shows the phase shift ratio for a set of measurements obtained at a diagnostic frequency of 168 GHz and 140 GHz. We note that the deviations observed at lower pressure result from in relatively large errors in the phase shift measurements at low electron density values. The ideal phase shift ratio is $168/140 = 1.2$ is achieved for a pressure up to 350 mbar, which shows that the electron density values are valid at least up to this pressure.

An abrupt deviation from ideal behavior is observed above 350 mbar, characterized by a 180 deg inversion of the phase shift (Fig. 12). The stable plasma conditions, signified by the plasma radius and gas temperature, suggests that the strong fluctuations in phase shift are a measurement artifact. Calculations of plane wave scattering around a dielectric cylinder, using the analytical solution provided by Balanis[43], shows that the measurement artifact

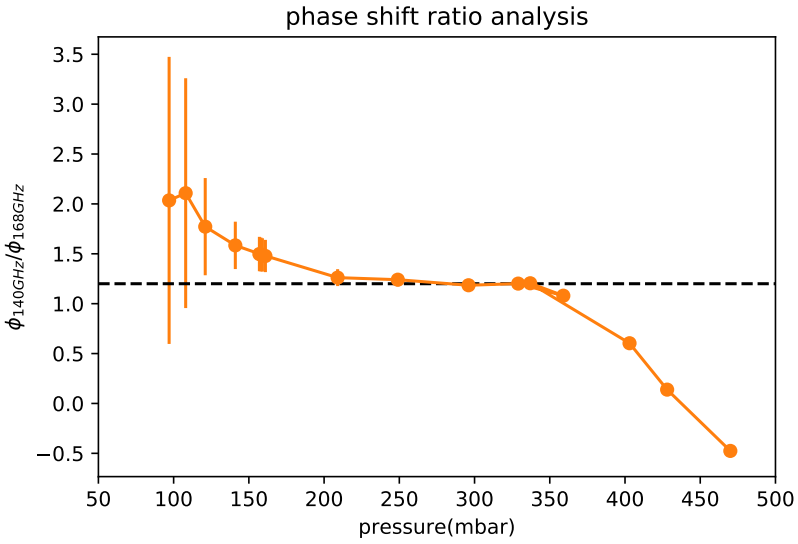

Figure 11: The ratio of phase shifts using 168 and 140 GHz diagnostic beams, indicating collisionless behavior between 100 mbar to 350 mbar.

can be explained by Mie-like scattering that occurs at a resonant condition of $\lambda_d/\mu \approx d_{\text{pl}}$. The calculations qualitatively capture the phase shift inversion at the estimated dielectric cylinder conditions.

The attenuation observed above 200 mbar, is associated with the beam scattering rather than the attenuation of the beam in the plasma medium. The phase shift ratio analysis demonstrates that the plasma has acts as a low-loss medium. We conclude that the homogeneous approximation give reliable electron density values for pressures below 350 mbar. Evidently, this is not a fundamental limit but rather a result of the experimental configuration in combination with the plasma conditions.

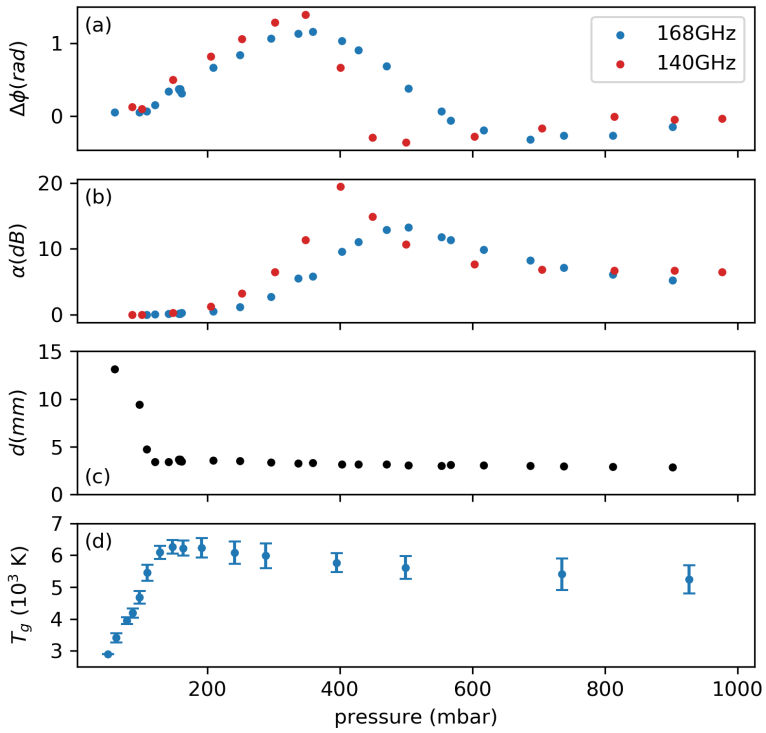

Figure 12: Propagation characteristics of the diagnostic beam terms of phase shift (a) and attenuation (b), and the corresponding plasma radius (c) and temperature (d) for the entire considered pressure range.